Biomedical Optics EXPRESS

Quantitative imaging of light-triggered doxorubicin release

Jeremy Kress,[1,2] Daniel J. Rohrbach,[1,2] Kevin A. Carter,[1] Dandan Luo,[1] Shuai Shao,[1] Shashikant Lele,[3] Jonathan F. Lovell,[1] and Ulas Sunar[1,2,*]

[1]*Department of Biomedical Engineering, University at Buffalo, Buffalo, NY, USA*
[2]*Department of Biomedical, Industrial & Human Factors Engineering, Wright State University, Dayton, OH, USA*
[3]*Department of Medicine, Roswell Park Cancer Institute, Buffalo, NY, USA*
[*]*ulas.sunar@wright.edu*

Abstract: The efficacy of chemotherapy is related, in large part, to the concentration of drug that reaches tumor sites. Doxorubicin (DOX) is a common anti-cancer drug that is also approved for use in liposomal form for the treatment of ovarian cancer. We recently developed a porphyrin-phospholipid (PoP)-liposome system that enables on demand release of DOX from liposomes using near infrared irradiation to improve DOX bioavailability. Owing to its intrinsic fluorescence, it is possible, and desirable, to quantify DOX concentration and distribution, preferably noninvasively. Here we quantified DOX distribution following light-triggered drug release in phantoms and an animal carcass using spatial frequency domain imaging. This study demonstrates the feasibility of non-invasive quantitative mapping of DOX distributions in target areas.

©2015 Optical Society of America

OCIS codes: (170.0110) Imaging systems; (170.3880) Medical and biological imaging; (170.0170) Medical optics and biotechnology; (170.6935) Tissue characterization.

References and links

1. M. Longmire, N. Kosaka, M. Ogawa, P. L. Choyke, and H. Kobayashi, "Multicolor in vivo targeted imaging to guide real-time surgery of HER2-positive micrometastases in a two-tumor coincident model of ovarian cancer," Cancer Sci. **100**(6), 1099–1104 (2009).
2. I. Rizvi, J. P. Celli, C. L. Evans, A. O. Abu-Yousif, A. Muzikansky, B. W. Pogue, D. Finkelstein, and T. Hasan, "Synergistic enhancement of carboplatin efficacy with photodynamic therapy in a three-dimensional model for micrometastatic ovarian cancer," Cancer Res. **70**(22), 9319–9328 (2010).
3. G. M. van Dam, G. Themelis, L. M. A. Crane, N. J. Harlaar, R. G. Pleijhuis, W. Kelder, A. Sarantopoulos, J. S. de Jong, H. J. G. Arts, A. G. J. van der Zee, J. Bart, P. S. Low, and V. Ntziachristos, "Intraoperative tumor-specific fluorescence imaging in ovarian cancer by folate receptor-α targeting: first in-human results," Nat. Med. **17**(10), 1315–1319 (2011).
4. T. M. Allen and P. R. Cullis, "Liposomal drug delivery systems: from concept to clinical applications," Adv. Drug Deliv. Rev. **65**(1), 36–48 (2013).
5. A. N. Gordon, J. T. Fleagle, D. Guthrie, D. E. Parkin, M. E. Gore, and A. J. Lacave, "Recurrent epithelial ovarian carcinoma: a randomized phase III study of pegylated liposomal doxorubicin versus topotecan," J. Clin. Oncol. **19**(14), 3312–3322 (2001).
6. S. D. Li and L. Huang, "Pharmacokinetics and biodistribution of nanoparticles," Mol. Pharm. **5**(4), 496–504 (2008).
7. K. A. Carter, S. Shao, M. I. Hoopes, D. Luo, B. Ahsan, V. M. Grigoryants, W. Song, H. Huang, G. Zhang, R. K. Pandey, J. Geng, B. A. Pfeifer, C. P. Scholes, J. Ortega, M. Karttunen, and J. F. Lovell, "Porphyrin-phospholipid liposomes permeabilized by near-infrared light," Nat. Commun. **5**, 3546 (2014).
8. S. Ibsen, E. Zahavy, W. Wrasidlo, T. Hayashi, J. Norton, Y. Su, S. Adams, and S. Esener, "Localized in vivo activation of a photoactivatable doxorubicin prodrug in deep tumor tissue," Photochem. Photobiol. **89**(3), 698–708 (2013).
9. H. Godoy, P. Vaddadi, M. Cooper, P. J. Frederick, K. Odunsi, and S. Lele, "Photodynamic therapy effectively palliates gynecologic malignancies," Eur. J. Gynaecol. Oncol. **34**(4), 300–302 (2013).
10. T. M. Baran and T. H. Foster, "Recovery of intrinsic fluorescence from single-point interstitial measurements for quantification of doxorubicin concentration," Lasers Surg. Med. **45**(8), 542–550 (2013).

#242127 Received 1 Jun 2015; revised 22 Jul 2015; accepted 16 Aug 2015; published 25 Aug 2015

11. G. M. Palmer, R. J. Boruta, B. L. Viglianti, L. Lan, I. Spasojevic, and M. W. Dewhirst, "Non-invasive monitoring of intra-tumor drug concentration and therapeutic response using optical spectroscopy," J. Control. Release **142**(3), 457–464 (2010).
12. A. Bogaards, H. J. Sterenborg, J. Trachtenberg, B. C. Wilson, and L. Lilge, "In vivo quantification of fluorescent molecular markers in real-time by ratio imaging for diagnostic screening and image-guided surgery," Lasers Surg. Med. **39**(7), 605–613 (2007).
13. A. Kim, M. Khurana, Y. Moriyama, and B. C. Wilson, "Quantification of in vivo fluorescence decoupled from the effects of tissue optical properties using fiber-optic spectroscopy measurements," J. Biomed. Opt. **15**(6), 067006 (2010).
14. U. Sunar, D. Rohrbach, N. Rigual, E. Tracy, K. Keymel, M. T. Cooper, H. Baumann, and B. H. Henderson, "Monitoring photobleaching and hemodynamic responses to HPPH-mediated photodynamic therapy of head and neck cancer: a case report," Opt. Express **18**(14), 14969–14978 (2010).
15. C. Sheng, B. W. Pogue, E. Wang, J. E. Hutchins, and P. J. Hoopes, "Assessment of photosensitizer dosimetry and tissue damage assay for photodynamic therapy in advanced-stage tumors," Photochem. Photobiol. **79**(6), 520–525 (2004).
16. R. Weersink, M. S. Patterson, K. Diamond, S. Silver, and N. Padgett, "Noninvasive measurement of fluorophore concentration in turbid media with a simple fluorescence /reflectance ratio technique," Appl. Opt. **40**(34), 6389–6395 (2001).
17. S. K. Chang, N. Marin, M. Follen, and R. Richards-Kortum, "Model-based analysis of clinical fluorescence spectroscopy for in vivo detection of cervical intraepithelial dysplasia," J. Biomed. Opt. **11**(2), 024008 (2006).
18. J. C. Finlay and T. H. Foster, "Recovery of hemoglobin oxygen saturation and intrinsic fluorescence with a forward-adjoint model," Appl. Opt. **44**(10), 1917–1933 (2005).
19. J. Wu, M. S. Feld, and R. P. Rava, "Analytical model for extracting intrinsic fluorescence in turbid media," Appl. Opt. **32**(19), 3585–3595 (1993).
20. K. R. Diamond, M. S. Patterson, and T. J. Farrell, "Quantification of fluorophore concentration in tissue-simulating media by fluorescence measurements with a single optical fiber," Appl. Opt. **42**(13), 2436–2442 (2003).
21. N. N. Zhadin and R. R. Alfano, "Correction of the internal absorption effect in fluorescence emission and excitation spectra from absorbing and highly scattering media: theory and experiment," J. Biomed. Opt. **3**(2), 171–186 (1998).
22. C. Liu, N. Rajaram, K. Vishwanath, T. Jiang, G. M. Palmer, and N. Ramanujam, "Experimental validation of an inverse fluorescence Monte Carlo model to extract concentrations of metabolically relevant fluorophores from turbid phantoms and a murine tumor model," J. Biomed. Opt. **17**(7), 077012 (2012).
23. R. B. Saager, D. J. Cuccia, S. Saggese, K. M. Kelly, and A. J. Durkin, "Quantitative fluorescence imaging of protoporphyrin IX through determination of tissue optical properties in the spatial frequency domain," J. Biomed. Opt. **16**(12), 126013 (2011).
24. U. Sunar, D. J. Rohrbach, J. Morgan, N. Zeitouni, and B. W. Henderson, "Quantification of PpIX concentration in basal cell carcinoma and squamous cell carcinoma models using spatial frequency domain imaging," Biomed. Opt. Express **4**(4), 531–537 (2013).
25. B. Yang, M. Sharma, and J. W. Tunnell, "Attenuation-corrected fluorescence extraction for image-guided surgery in spatial frequency domain," J. Biomed. Opt. **18**(8), 080503 (2013).
26. J. F. Lovell, C. S. Jin, E. Huynh, H. Jin, C. Kim, J. L. Rubinstein, W. C. W. Chan, W. Cao, L. V. Wang, and G. Zheng, "Porphysome nanovesicles generated by porphyrin bilayers for use as multimodal biophotonic contrast agents," Nat. Mater. **10**(4), 324–332 (2011).
27. D. J. Cuccia, F. Bevilacqua, A. J. Durkin, F. R. Ayers, and B. J. Tromberg, "Quantitation and mapping of tissue optical properties using modulated imaging," J. Biomed. Opt. **14**(2), 024012 (2009).
28. C. M. Gardner, S. L. Jacques, and A. J. Welch, "Fluorescence spectroscopy of tissue: recovery of intrinsic fluorescence from measured fluorescence," Appl. Opt. **35**(10), 1780–1792 (1996).
29. A. Gabizon, D. Goren, A. T. Horowitz, D. Tzemach, A. Lossos, and T. Siegal, "Long-circulating liposomes for drug delivery in cancer therapy: a review of biodistribution studies in tumor-bearing animals," Adv. Drug Deliv. Rev. **24**(2-3), 337–344 (1997).
30. W. Mo, D. Rohrbach, and U. Sunar, "Imaging a photodynamic therapy photosensitizer in vivo with a time-gated fluorescence tomography system," J. Biomed. Opt. **17**(7), 071306 (2012).
31. M. S. Ozturk, D. Rohrbach, U. Sunar, and X. Intes, "Mesoscopic fluorescence tomography of a photosensitizer (HPPH) 3D biodistribution in skin cancer," Acad. Radiol. **21**(2), 271–280 (2014).
32. D. S. Kepshire, S. L. Gibbs-Strauss, J. A. O'Hara, M. Hutchins, N. Mincu, F. Leblond, M. Khayat, H. Dehghani, S. Srinivasan, and B. W. Pogue, "Imaging of glioma tumor with endogenous fluorescence tomography," J. Biomed. Opt. **14**(3), 030501 (2009).
33. K. R. Rollakanti, S. C. Kanick, S. C. Davis, B. W. Pogue, and E. V. Maytin, "Techniques for fluorescence detection of protoporphyrin IX in skin cancers associated with photodynamic therapy," Photonics Lasers Med. **2**(4), 287–303 (2013).
34. S. Gioux, A. Mazhar, D. J. Cuccia, A. J. Durkin, B. J. Tromberg, and J. V. Frangioni, "Three-dimensional surface profile intensity correction for spatially modulated imaging," J. Biomed. Opt. **14**(3), 034045 (2009).
35. T. Wu, J. Qu, T. H. Cheung, K. Lo, and M. Y. Yu, "Preliminary study of detecting neoplastic growths in vivo with real time calibrated autofluorescence imaging," Opt. Express **11**(4), 291–298 (2003).

#242127 Received 1 Jun 2015; revised 22 Jul 2015; accepted 16 Aug 2015; published 25 Aug 2015
(C) 2015 OSA

36. J. Y. Qu, Z. Huang, and J. Hua, "Excitation-and-collection geometry insensitive fluorescence imaging of tissue-simulating turbid media," Appl. Opt. **39**(19), 3344–3356 (2000).
37. T. M. Baran and T. H. Foster, "New Monte Carlo model of cylindrical diffusing fibers illustrates axially heterogeneous fluorescence detection: simulation and experimental validation," J. Biomed. Opt. **16**(8), 085003 (2011).
38. Q. Fang and D. A. Boas, "Monte Carlo simulation of photon migration in 3D turbid media accelerated by graphics processing units," Opt. Express **17**(22), 20178–20190 (2009).

1. Introduction

One of the main challenges in the treatment of advanced ovarian cancer is the presence of disseminated microscopic residual nodules. Recent efforts have aimed at diagnosing and treating these [1–3]. Incomplete surgical resection can lead to recurrence. Chemotherapy plays a major role and nanocarriers such as liposomes have been developed to enhance the biodistribution and anti-cancer efficacy of various drugs [4]. Liposomal doxorubicin is used in patients with recurrent ovarian carcinoma resistant to first-line platinum-based chemotherapy agents [5]. However, drug delivery must overcome physiological barriers and release the nanocarrier contents in the tumor [6]. To improve biodistribution and bioavailability, we recently developed porphyrin-phospholipid (PoP) liposomes that can be permeabilized on demand with near infrared (NIR) light, with excellent temporal and spatial control [7].

By restricting drug delivery to a specified region, injected doses, and therefore systemic side effects, can be reduced. PoP-liposomes hold great potential for this, with the ultimate goal to allow the clinician to restrict light irradiation to the tumor sites to activate release of doxorubicin at a specified site and desired time [8]. This approach somewhat resembles photodynamic therapy (PDT) that has been explored in the clinic for recurrent gynecologic malignancies [9]. Similar to PDT, the trigger light can be delivered via wide-field illumination or endoscopic approach for releasing the active DOX at tumor sites in the intraperitoneal cavity.

An image-guided approach to the local delivery of chemotherapies is desirable, as it allows for the evaluation of any drug-related effects in the surrounding healthy tissues. To achieve this goal, knowledge of the local DOX concentration in the target tissue is essential. Preferably this information about drug concentration and distribution could be obtained noninvasively at the bedside. Since DOX fluoresces, fluorescence spectroscopy or imaging can be implemented for quantification of DOX content *in vivo* [10, 11]. However, the raw fluorescence signal is known to be strongly affected by tissue optical absorption and scattering properties, and thus is not related to the true DOX concentration. Several spectroscopic methods have been utilized for quantification of drug concentration *in vivo* [8, 10–22].

Here we apply spatial frequency domain imaging technique for quantification of absolute DOX fluorescence concentration by compensating the variations in fluorescence signal due to absorption and scattering at both excitation and emission wavelengths [23–25]. We explored the accuracy of quantification in tissue simulating phantoms and in a mouse. We then investigated the time-dependent release kinetics with respect to trigger light energy. This study demonstrates the localized NIR light triggering based photoactivation of DOX with noninvasive, quantitative measures.

2. Materials and methods

2.1 Preparation of DOX in PoP-liposomes

PoP-liposomes were synthesized from pyro-lipid generated in a manner as we have previously described [26] through esterification of pyro with lyso-C16-PC, using 1-Ethyl-3-(3-dimethylaminopropyl)carbodiimide (EDC) and 4-dimethylaminopyridine (DMAP) in chloroform. PoP-liposomes are formed by dispersing porphyrin-lipid, PEGylated-lipid, cholesterol, and distearoylphosphatidylcholine in chloroform then evaporating the solvent. A

#242127 Received 1 Jun 2015; revised 22 Jul 2015; accepted 16 Aug 2015; published 25 Aug 2015
(C) 2015 OSA

20 mg/mL lipid solution of was extruded with a high pressure lipid extruder with a 250 mM ammonium sulfate solution. Polycarbonate membranes of 0.2, 0.1 and 0.08 μm pore size are sequentially stacked and passed through the extruder 10 times. Free ammonium sulfate was removed by overnight dialysis in a 10% sucrose solution with 10 mM HEPES pH 7. DOX (LC Labs) is then loaded by incubating at 60 °C for 1 hour. Loading tests using G-75 columns showed that the loading efficacy in all DOX loaded samples was greater than 95%. 480 nm excitation and 590 nm emission was used to detect DOX in a fluorescence plate reader (TECAN Safire). PoP-liposome self-assembly status and elution position can also be tracked without interference by using 420 nm excitation and 670 nm emission for the PoP.

2.2 Custom SFDI imaging and release setup

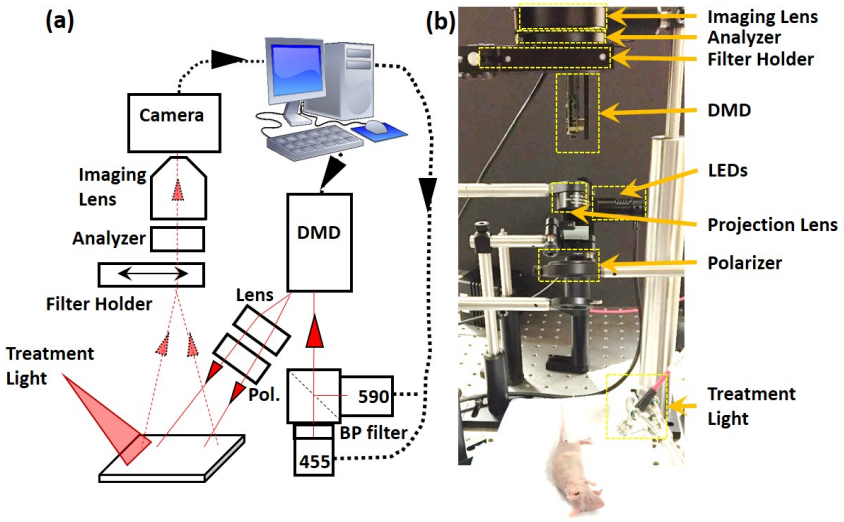

Fig. 1. The experimental setup. (a) The system uses two LEDs (455 nm with a 20 nm band-pass filter and 590 nm) directed onto a DMD to project images of varying spatial frequencies onto tissue simulating phantoms or tissue (Target). The reflected light field is captured by an EMCCD camera with adjustable filters to selectively capture emission and excitation light. Crossed linear polarizers reduced specular reflection. (b) The picture of the setup.

Figure 1(a) shows the detailed schematic diagram and (b) shows the picture of our custom spatial frequency domain imaging (SFDI) setup. The setup consisted of a Digital Micro-mirror Device (DMD) from a modified projector (Lightcrafter, Logic PD Inc, MN) to spatially modulate the light into the desired frequency and phase pattern. The setup had two high-power, compact Light-Emitting Diodes (LEDs), LCS series, each centered at 455 nm and 590 nm, both from Mightex, CA. The 455 nm LED light was bandpass-filtered at 455 nm ± 20 nm for imaging DOX optical properties at the excitation peak as well as exciting DOX fluorescence. The 590 nm LED was used to measure optical properties at the emission peak. LED light beam was directed to a projector with a DMD module having 608 x 684 pixel resolution. The DMD module generated the appropriate sine wave patterns with three different phases (0, $2\pi/3$, $4\pi/3$) and eleven spatial frequencies from 0 to 5.8 cm^{-1}. The patterns were projected onto the surface and reflected light was collected with the high sensitive EMCCD camera (1004 x 1002 pixels, Luca, Andor, Belfast, Ireland). The camera was focused on the same field of view the projector was illuminating (2.5 cm x 2.5 cm, camera; 2.5 cm x 1.4 cm, DMD). The CCD acquisition time was set to 0.2 s in reflectance mode, 2.0 s in fluorescence mode. A two-position filter holder in front of the camera lens held a 530 nm long pass filter and a 590 nm ± 20 nm band-pass filter for fluorescence measurements and no filter was used for reflectance measurements. Cross-polarizers in front of the projector and

#242127 Received 1 Jun 2015; revised 22 Jul 2015; accepted 16 Aug 2015; published 25 Aug 2015
(C) 2015 OSA

camera rejected specular reflection during reflectance imaging. For the release experiments, the treatment light was a 665 nm laser with a fluence rate of 350 mW/cm^2 and the diameter of the beam was adjusted for each application. The entire system was automated by a custom LabVIEW software program.

2.3 Model for reflectance and fluorescence analysis

Bulk optical absorption (μ_a) and scattering (μ_s') parameters were quantified by fitting spatial frequency domain reflectance ($R_d(f)$) data with a modified frequency-domain Monte Carlo model by using a reference phantom with known optical properties by using custom Matlab program with the lsqcurvefit nonlinear fitting algorithm [27]. Two different initial conditions were used to check for possible local minima. To quantify absorption and scattering parameters, 5 spatial frequencies from 0 to 2.25 cm^{-1} and three phases (0, 2π/3, 4π/3) were used.

The quantification DOX fluorescence concentration was performed by utilizing the Gardner model that corrects raw fluorescence signal by compensating for optical absorption (μ_a) and scattering (μ_s') loss both at excitation and emission wavelengths [23, 24, 28]. In this model, the fluorescence correction factor, $X_{1D}(\lambda_{ex},\lambda_{em})$, is determined by using the quantified optical parameters from SFDI measurements, where $X_{1D}(\lambda_{ex},\lambda_{em})$ represents the effective path-length during excitation light penetrating into and escape of the emitted fluorescence from the tissue. Then we calculated the corrected fluorescence as $F_{corr} = F_{raw} / X_{1D}$, where F_{raw} is the measured raw signal, X_{1D} is the correction factor and F_{corr} is the corrected fluorescence by compensating the optical absorption, scattering and light propagation. By using the calibration factor, transition to DOX concentrations is established.

2.4 Phantom preparation and animal study

Phantoms were prepared using Intralipid 20% (Fresenius Kabi) for scattering and India Ink (Higgins) for absorption. Four phantoms were prepared with different combinations of optical properties: μ_a = 0.5 and 1.5 cm^{-1}, μ_s' = 20 and 30 cm^{-1} at 455 nm; μ_a = 0.4 and 1.2 cm^{-1}, μ_s' = 15.8 and 23.8 cm^{-1} at 590 nm. Each phantom had a total volume of 120 mL. For the calibration of DOX concentration, a stock solution of 0.5 mg/mL free-DOX was used. After baseline SFDI and fluorescence measurements of each phantom, increasing volumes of free-Dox were added to each (400, 800, 1200, 1600 and 2000 μL) with SFDI and fluorescence measurements acquired at each addition.

DOX release was performed in phantoms prepared as above with μ_s' = 20 cm^{-1} and μ_a = 0.5 and 1.0 cm^{-1} at 455 nm and a total volume of 70 mL. A stock solution of 2.59 mg/mL PoP liposomes was prepared as described in the previous section. The phantom was placed on a stir plate set to 15 rpm. SFDI and fluorescence measurements were acquired before and after the addition of PoP liposomes (200 μL). The stir plate was increased to 30 rpm and the treatment light (1.72 cm diameter spot) was turned on. Fluorescence measurements were acquired every 4 minutes.

A recently sacrificed nude mouse was acquired for simulated *in vivo* measurements. The mouse was placed on the imaging plane of the SFDI setup with the injection site near the center of the field of view and SFDI-fluorescence measurements were acquired. The mouse was injected subcutaneously with 50 μL of a lightly scattering medium (μ_s' = 5 cm^{-1} at 455 nm) containing 22 μg/mL PoP-Liposomes to simulate heterogeneity under the surface and SFDI-fluorescence measurements were performed again. The treatment light (1.0 cm diameter) was directed onto the injection site, covering it completely. Fluorescence measurements were acquired every 5 minutes to assess the release dynamics during treatment.

#242127 Received 1 Jun 2015; revised 22 Jul 2015; accepted 16 Aug 2015; published 25 Aug 2015
(C) 2015 OSA

3. Results and discussion

3.1 System calibration

The system was characterized with multiple phantoms made by titrating the optical properties. The mean percent error in quantifying the absorption parameter was 6.3% with a maximum of 18.0% and the mean percent error for scattering parameter was 6.4% with a maximum of 12.8%. Similarly, fluorescence phantoms were prepared by titrating the DOX concentration. Reconstructed raw fluorescence values with respect to concentration were used as a calibration curve to obtain absolute DOX concentrations.

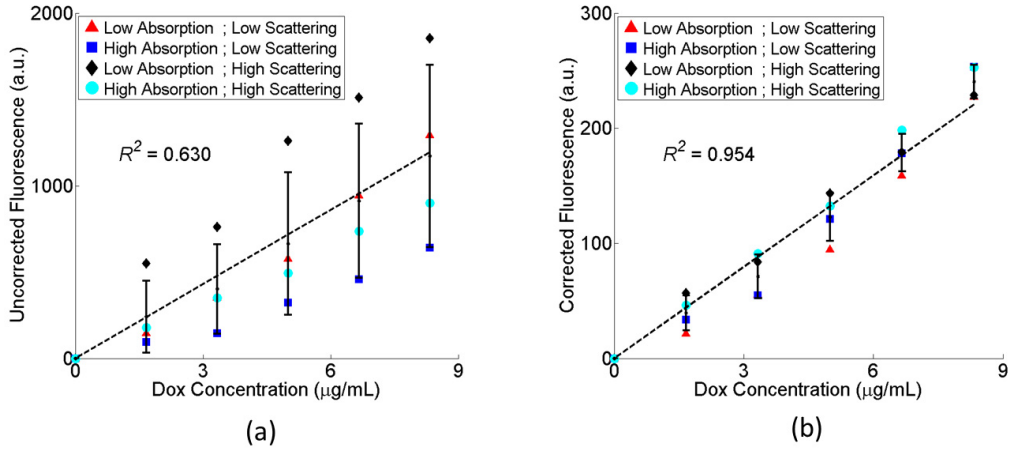

Fig. 2. (a) Uncorrected (raw) DOX fluorescence vs DOX concentration (b) Attenuation corrected DOX fluorescence vs DOX concentration using all phantoms at different absorption and scattering parameters. Error bars represent the standard deviation of the four phantoms at different concentrations.

Figure 2 shows the raw fluorescence intensity with respect to DOX concentrations (0, 1.67, 3.33, 5.00, 6.67, 8.33 μg/mL) at different optical parameter ranges of μ_a = 0.50 cm^{-1} and 1.5 cm^{-1} and μ'_s = 20 cm^{-1} and 30 cm^{-1}. We choose 80 × 40 pixel region of interest (ROI) for the target area defined by the threshold determined by the intensity counts equal or above the 50% of the peak intensity. Mean values of each ROI intensity counts (a.u.) were plotted with respect to the concentration, as well as the mean and standard deviation of the four phantoms at different concentrations, as shown in Fig. 2. The raw fluorescence signal showed substantial variations with respect to optical parameters (Fig. 2(a)), but attenuation corrected fluorescence showed much less variation with respect to DOX concentration (Fig. 2(b)). The uncorrected raw fluorescence signals had a poor correlation with the DOX concentration (r^2 = 0.630), which improved greatly with the corrected fluorescence signal (r^2 = 0.954).

To determine the accuracy of our system at quantifying DOX concentration, two phantoms were made with μ_a = 3 cm^{-1} and μ_s' = 20 cm^{-1} or 40 cm^{-1}. DOX was added in 1 μg/mL increments to give final concentrations of 1, 2, 3 and 4 μg/mL for each phantom. Our system was able to determine the DOX concentration with a mean percent error of 15.6% with a maximum error of 44.0% at the lowest concentration. In preclinical human xenograft models, it is established that therapeutic doses lead to liposomal doxorubicin accumulation at concentrations between 10 and 40 μg/mL in tumor tissue based on the density of tissue being 1 mg/mL [29]. This corresponds to concentrations well above the lowest dose we tested. If

#242127 Received 1 Jun 2015; revised 22 Jul 2015; accepted 16 Aug 2015; published 25 Aug 2015
(C) 2015 OSA

the lowest concentration (1 μg/mL), which is at least 10x lower than in vivo concentration, is excluded, then the mean error is 9.6% with a maximum of 19.0%. These results highlight the accuracy of our system at extracting [DOX] as well as the clinical relevancy.

3.2 DOX imaging contrast

Figure 3 shows representative images of phantoms with the same amount of DOX (200 μL of drug added, equivalent to 7.4 μg/mL DOX concentration)) but different optical absorption parameters (μ_a); the first phantom (upper phantom in Fig. 3(a)) had μ_a = 0.5 cm^{-1}, while the second one (lower phantom, Fig. 3(a)) had μ_a = 1.0 cm^{-1} while the scattering parameters were fixed (μ'_s = 20 cm^{-1}). The uncorrected fluorescence image (Fig. 3(b)) shows a high DOX fluorescence signal for the low absorbing phantom compared to the high absorbing one (1955 ± 101 a.u. vs. 1149 ± 54 a.u. respectively), due to less light attenuation. Thus the image contrast was lower in high absorbing phantom. However, the corrected DOX concentration maps (Fig. 3(c)) show similar values and contrast for both phantoms in the ROI (12.8 ± 0.56 μg/mL and 13.0 ± 0.58 μg/mL, respectively).

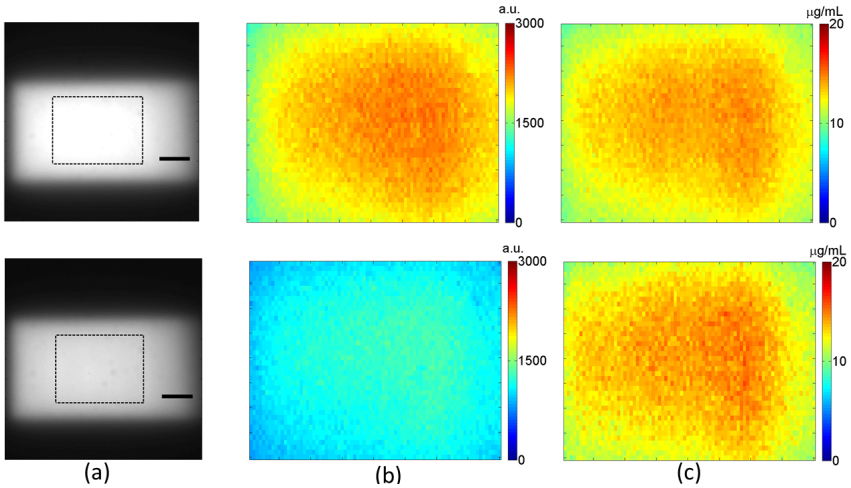

Fig. 3. Representative images of phantom with different optical properties of μ_a = 0.5 cm^{-1} (a-upper phantom), and μ_a = 1.0 cm^{-1} (b-lower phantom). (a) White light structural image of low-absorbing phantom (upper) and higher absorbing phantom (lower) (b) Uncorrected DOX fluorescence image from a phantom with the same added concentration (c) DOX fluorescence concentration indicating similar contrast.

Next we studied DOX imaging contrast in a hairless mouse carcass. Figure 4(a) shows the white light structural image showing the PoP injected and DOX released site. The treatment light illuminated the injection site for 60 minutes. As the uncorrected fluorescence (Fig. 4(b)) and concentration (Fig. 4(c)) maps indicates the distribution of the image contrasts were different, possibly due to optical parameter differences, mainly due to scattering parameter differences between the skin vs Intralipid. We also note that the autofluorescence was subtracted from the total fluorescence signal in order to quantify DOX contribution. We estimated the autofluorescence signal accounts for ~63% of the initial background signal prior to treatment and ~12% of the maximum fluorescence signal during treatment.

#242127 Received 1 Jun 2015; revised 22 Jul 2015; accepted 16 Aug 2015; published 25 Aug 2015
(C) 2015 OSA

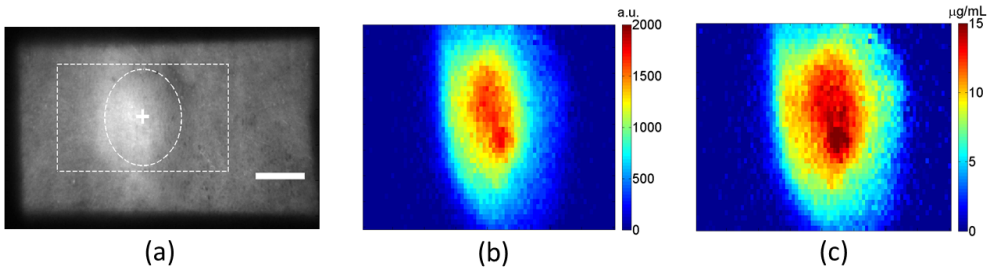

Fig. 4. Representative DOX quantification in a mouse carcass. (a) White light image showing the structure of the PoP injection and release site. (b) Uncorrected DOX fluorescence image after 60-minute illumination. (c) DOX concentration image after 60-minute illumination.

3.3 DOX release kinetics

Figure 5 shows the DOX release kinetics in phantoms with respect to uncorrected DOX fluorescence (Fig. 5(a)), corrected DOX fluorescence (Fig. 5(b)) and quantified DOX concentration values (Fig. 5(c)). Error bar sizes shown in Figs. 5(a) and 5(b) correspond to one standard deviation in the cropped images while in Fig. 5(c) the error bars incorporate the additional uncertainty in the calibration factor shown in Fig. 2(b). There is a significant time delay for full release in the higher absorbing phantom (68 min versus 48 min). We expect that the treatment light did not probe the whole prodrug (PoP) volume, especially for the case of high absorbing phantom. This characteristic is controlled by fluence rate and light penetration depth (partial volume effect). It is interesting to note that from Fig. 5(a) one could wrongly infer that the release of bioavailable DOX was still incomplete by 68 min, but the corrected DOX fluorescence (Fig. 5(b)) and the quantified DOX concentration release (Fig. 5(c)) indicate that 68 min of treatment light irradiation was almost enough for both phantoms to have complete release. These results imply that in certain cases quantification of the released (bioavailable) DOX concentration could be crucial to accurately treat tumors for individualized optimization.

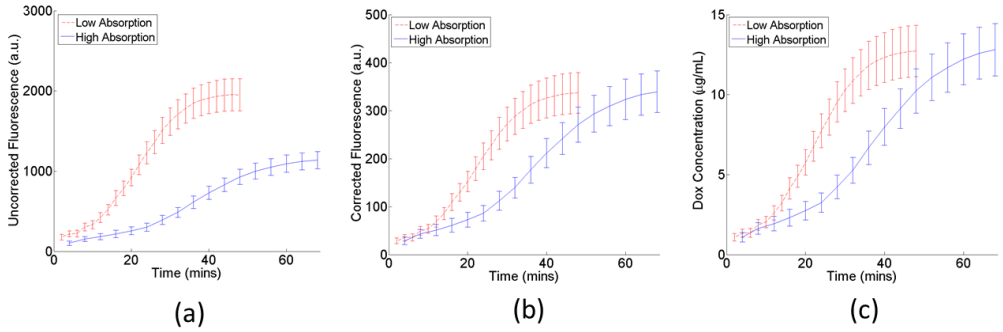

Fig. 5. DOX release kinetics in phantoms. (a) The release characterized by uncorrected fluorescence changes. (b) The release characterized by corrected fluorescence changes. (c) The release characterized by the quantified DOX concentration changes.

We then investigated the DOX release kinetics in a mouse carcass (Fig. 6). Figure 6(a), 6(b), and 6(c) shows measured DOX concentrations at pre-treatment, 10 min post- and 60 min post-treatment laser illumination time points, respectively, with an increasing trend during the treatment from 3.54 ± 0.49 μg/mL (pre-release) to 13.42 ± 2.2 μg/mL (60 min post-treatment). We observed that the total DOX concentration shown in Fig. 6(d) did not reach the injected amount (equivalent to ~22 μg/mL of DOX concentration). This is likely due to the overlying skin and shallow penetration depth of excitation light. We again expect that the full drug volume was not probed by the treatment light due to partial volume effect

#242127 Received 1 Jun 2015; revised 22 Jul 2015; accepted 16 Aug 2015; published 25 Aug 2015
(C) 2015 OSA

originating from the skin layer and inhomogeneous distribution of the prodrug PoP under the skin. Some fraction of the total volume and near the surface could be released and then gradually mixed with the untreated volume.

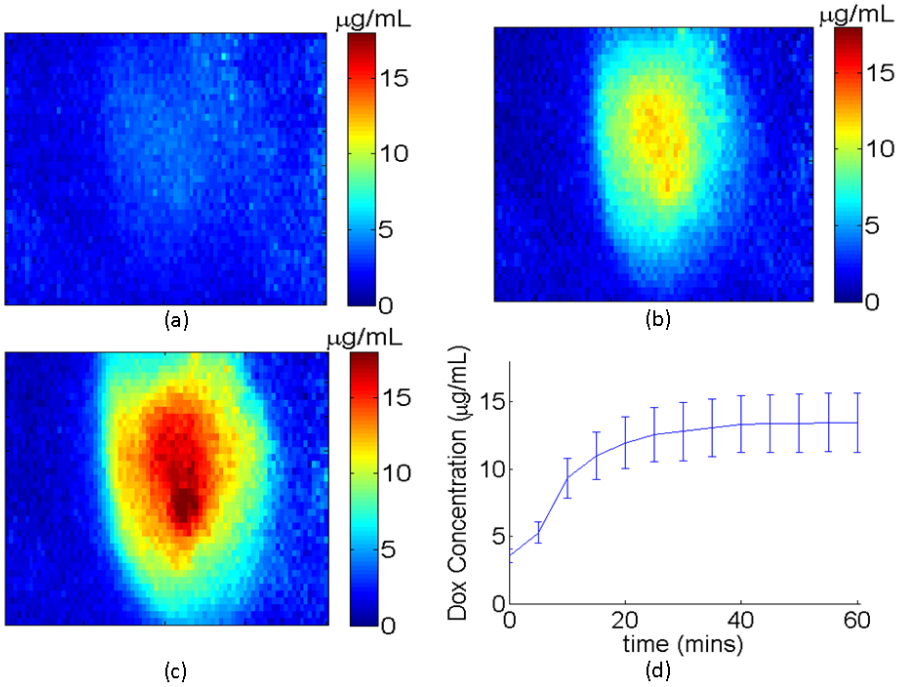

Fig. 6. DOX release kinetics in a mouse carcass. (a) Pre-treatment (b) 10 min post-treatment (c) 60 min post-treatment. (d) Complete DOX release kinetics curve with mean and standard deviation of the ROI.

Accurate, quantitative information is important in triggered delivery systems, like the light-triggered liposomes, to ensure the expected amount and appropriately timed drug release is occurring. The targeted release ensures that minimal DOX is released near healthy tissue to minimize the adverse effects common with systemic chemotherapy. In this study the target was on or near the surface and therefore light could easily be directed to the desired area. However, in the peritoneal cavity wide-field light delivery is not always possible. Fortunately, alternative modes of light delivery such as interstitial fiber-optics or endoscopes will also work for drug release. 3D fluorescence imaging would also provide more accurate approach to reduce or eliminate partial volume effects such as those originating from skin layers *in vivo* [30–33].

The SFDI algorithm assumes a flat, 2D surface, and any deviation from this will affect the quantification of optical properties as well as the fluorescence. In this study, the tissue simulating phantoms had flat surfaces and great care was taken to position the mouse such that the surface of the imaged area was as flat as possible. However, due to 3D nature of the mouse surface we expect there are inherent curvature effects that would lead to quantification errors. Efficiently compensating for curvature effects is ongoing research that several groups have been investigating. One quantitative approach explored by Gioux *et al.* used 3D surface profilometry to correct the diffuse reflectance intensity [34]. This technique allowed for accurate optical property quantification for phantoms with surface height variations of up to 3 cm and tilt angle up to 40°. Other approaches used semi-quantitative but clinically practical ratiometric methods such as the ratio of fluorescence signal to reflectance signal to eliminate or reduce geometric as well as optical parameter dependency on the quantification of optical

#242127 Received 1 Jun 2015; revised 22 Jul 2015; accepted 16 Aug 2015; published 25 Aug 2015
(C) 2015 OSA

parameters and drug concentration [35, 36]. These points are being investigated in our endoscopic design for internal organs such as ovarian tissue. We are implementing a fast and efficient version of the approach explored by Gioux *et al*. [34], since it is a robust and quantitative approach directly applicable to our instrument.

It should be noted that the post-processing takes about 5 minutes depending on the pixel binning. Utilizing GPU based fast Monte Carlo model (e.g [37, 38].) or analytical P3 approximation [18] for the pixel-based fitting can allow reducing the computation time and pixel binning for higher resolution applications such as endoscopic imaging in clinical settings. Ultimately, this can lead to real-time optimal light delivery according to DOX distributions.

In this study, the light dose was delivered uniformly across the treatment area and the fluence rate was chosen based on previous mouse studies. In areas with very heterogeneous optical properties, a uniform light dose may not be the best delivery option. Knowledge of the tissue optical properties and liposome distribution before light delivery, as well as the changes caused by triggered release, would allow for optimization on an individual basis. Our SFDI setup is well equipped to perform these measurements and we will be investigating optimized release in the future.

Optical methods are fast, mobile and can assess physiologic parameters and drug concentration at bedside with multiple time points to monitor changes over time. These changes in physiologic parameters and drug pharmacokinetics can inform on therapy response, allowing for early assessment of response and earlier re-intervention if necessary. In addition to clinical applications, optical methods such as SFDI can be used in the preclinical setting for the rapid testing of novel drugs prior to use in human subjects.

4. Conclusions

In conclusion, we utilized a custom SFDI system to quantify the absolute concentration of DOX in phantoms and in an animal carcass. We showed that SFDI could quantify DOX concentration distribution noninvasively. Noninvasive fast optical techniques enable the assessment of bioavailable drug in vivo and thus therapeutic activity and response. Ultimately, this will lead to optimization and control of drug release that may result in higher response rates and fewer side effects. The ability to characterize drug release makes SFDI potentially useful tool for evaluating and characterizing novel drug release and deliver *in vivo* for fast clinical translation.

Acknowledgments

We thank the funding support from National Institute of Biomedical Imaging and Bioengineering (NIBIB) R21-EB01914701. We also thank Dr. Rolf Saager in Dr. Anthony Durkin lab at University of California Irvine for providing the SFDI Monte Carlo code.

#242127 Received 1 Jun 2015; revised 22 Jul 2015; accepted 16 Aug 2015; published 25 Aug 2015
(C) 2015 OSA